INSTRUMENTATION

Image Improvement and Design Optimization of the Time-of-Flight PET

Wai-Hoi Wong, Nizar A. Mullani, Edouard A. Philippe, Ross Hartz, and K. Lance Gould

University of Texas Health Science Center at Houston, Houston, Texas

Positron emission tomography (PET) with the added time-of-flight information has been shown to provide a better reconstructed image over conventional positron tomography. This improvement depends on the size of the object being imaged, the intrinsic resolution of the detector, and the time-of-flight resolution. Moreover, the signal-to-noise ratio of a PET image is related not only to the total number of counts in the image but also to the event-locating uncertainties, the reconstruction filter function, and the recovered resolution in the image. This study provides a physical explanation for, and description of, the improvement in signal-to-noise ratio of a reconstructed image as a function of the crucial design parameters: time-of-flight timing resolution, intrinsic detector resolution, object size, and reconstructed image resolution.

J Nucl Med 24: 52–60, 1983

Under the ideal situation of infinite counting statistics, a properly designed positron emission tomograph (PET) could reconstruct an accurate two-dimensional image. Under clinical circumstances, however, counting statistics are limited by the radiation dosage that can be safely administered to the patient, and the detector efficiency of the tomograph. Consequently, the limited counting statistics cause a noisy reconstructed image, where the amount of noise in the image is related to detector's uncertainty in exactly locating the emitting event along and normal to the direction of photon flight, and the filter function used in the reconstruction process. Recently it has been demonstrated (*1–4*) that the addition of time-of-flight (TOF) information, obtained by measuring the difference in the arrival times of the annhilation photons, provides a better signal-to-noise (S/N) ratio than that in conventional PET images. The TOF technique has been shown to improve the image signal-to-noise ratio by factors of 1.5 to 3, depending on the TOF resolution, compared with conventional systems with identical detector geometry and efficiency.

Received Feb. 18, 1982; revision accepted Sept. 13, 1982.

For reprints contact: Wai-Hoi Wong, PhD, Univ. of Texas Health Science Center at Houston, Div. of Cardiol., 6431 Fannin, 1.246 MSMB, Houston, TX 77030.

However, in order to realize the full benefit of added TOF information, it is necessary to relate the S/N improvement in the image to the detector's intrinsic resolution (IR), TOF timing resolution, reconstruction object size, and final reconstructed image resolution (RR). Such a comprehensive analysis should provide a better understanding of pertinent design parameters so that the design or selection of a PET camera can be tailored to individual, specific applications or requirements.

THEORY AND METHODS

In conventional PET, a coincidence event detected between a pair of detectors is assigned an equal probability of location along the coincidence line, since the position of the site of the annihilation is not known other than its being somewhere on the coincidence line. However, in TOF-PET, for each event detected, a measure of the time-of-flight difference between the two annihilation photons provides an approximate value for the position of the source. The position information thus obtained is associated with an uncertainty that depends on the properties of the detector and its associated electronics. This uncertainty can be measured by accumulating many detected events along the coincidence line. We have shown that it approximates a Gaussian

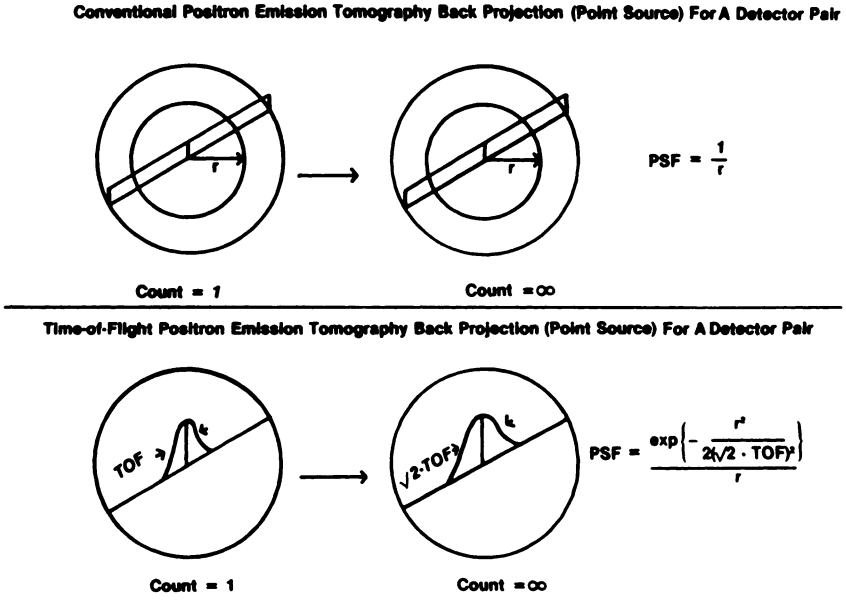

FIG. 1. Effect of carrying over of the confidence-weighted method used by conventional PET to TOF PET.

function, with the mean at the source of the positrons and a full width at half maximum (FWHM) of Δ_t (or standard deviation of σ_t). Location of a source based on the datum collected alone is called the most likely position (MLP), since every event detected represents a measure of the most likely position of the source.

It has also been shown that in reconstructing images from TOF information, signal-to-noise ratio is improved if each detected event is represented by its known uncertainty function (*3–5*). This is to decrease the noise band pass from that of the sampling pixel's size limit to that of the detection limit. Thus, each detected event is replaced by a one-dimensional Gaussian function along with the coincidence line with mean at the measured position and a standard deviation σ_t (Fig. 1). This technique has been called confidence weighting. In the conventional PET, the back-projection technique is a confidence weighting with infinitely large TOF uncertainty. The confidence weighting results in a convolution of the measured data with a noise-free probability function with a standard deviation of σ_t. A pictorial illustration of the confidence-weighting technique of the conventional and TOF PETs is shown in Fig. 1, assuming infinitesimally small σ_i. As the intrinsic resolution of detection σ_i becomes finite, such confidence weighting should incorporate the detector's intrinsic resolution uncertainty as well (*4*). This is also illustrated in appendix 1 by extending the argument in Ref. *3* to include the finite detector's size weighting. Hence, every measured count is replaced by a two-dimensional confidence function with one axis characterized by the TOF uncertainty and the other axis characterized by the detector's intrinsic uncertainty.

For the profile with the coincidence lines parallel to the x-axis and without 2-D confidence weighting, a point source at the center of field will be accumulated as a 2-D Gaussian p_0 (Fig. 2):

$$p_0 = \exp(-x^2/2\sigma_t^2) \times \exp(-y^2/2\sigma_i^2), \qquad (1)$$

since this function p_0 is also the 2-D uncertainty function used for the 2-D confidence weighting. The 2-D weighted point spread function p_1 for that profile is then given by:

$$p_1 = \begin{cases} p_0 ** p_0 & r \le D/2 \\ 0 & r > D/2 \end{cases} = \begin{cases} \exp\left(\dfrac{-x^2}{2\sigma_{ct}^2}\right) \cdot \exp\left(\dfrac{-y^2}{2\sigma_{ci}^2}\right) & r \le D/2 \\ 0 & r > D/2 \end{cases} \qquad (2)$$

where $\sigma_{ct} = \sqrt{2\sigma_t}$, $\sigma_{ci} = \sqrt{2\sigma_i}$, and D is the diameter of the reconstructed field size. The back-projected point spread function p(r) for a point source at the center is then given by the summation of all the projections:

$$p(r) = R\{p_1(r)\} = R\{p_0 ** p_0\} \qquad (3)$$

Where R is the back-projection operator.

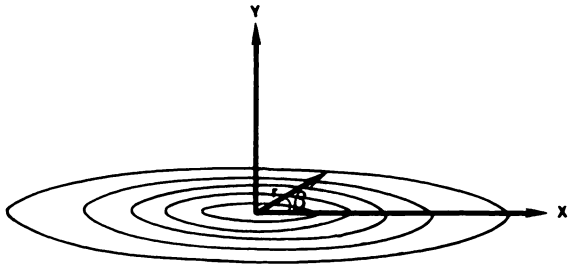

FIG. 2. Sampling isosensitivity contour of a pair of TOF detectors.

$$p(r) = \begin{cases} \int_0^{\pi} \exp\left(\frac{-r^2\cos^2\beta}{2\sigma_{ct}^2}\right) \\ \quad \cdot \exp\left(\frac{-r^2\sin^2\beta}{2\sigma_{ci}^2}\right) d\beta & r \le D/2 \\ 0 & r > D/2 \end{cases}$$

This prefiltered back-projected point spread function (BPSF) p(r, σ, σ_{ct}, D) is found to be (Appendix 2):

$$p = \begin{cases} \frac{I_0(qr^2)}{e^{sr^2}} & r \le D/2 \\ 0 & r > D/2, \end{cases} \quad (4)$$

where

$$s = \tfrac{1}{4}\left(\frac{1}{\sigma_{ci}^2} + \frac{1}{\sigma_{ct}^2}\right),$$

$$q = \tfrac{1}{4}\left(\frac{1}{\sigma_{ci}^2} - \frac{1}{\sigma_{ct}^2}\right),$$

and I_0 is the zeroth-order modified Bessel function of the first kind.

The cross section of BPSF is illustrated in Fig. 3, with time-of-flight FWHM, Δ_t, equal to 64 mm, detector intrinsic resolution FWHM, Δ_I, equal to 6.5 mm, and D greater than 30 cm. The figure also shows a back-projected point spread function in which a large time-of-flight value for Δ_t equal to 70 cm is used to simulate a non-TOF unfiltered back-projected PSF. As seen in Fig. 3, the TOF P(r) retains most of the activity in the peak region because p(r) converges to zero quite rapidly with respect to r, whereas the non-TOF unfiltered p(r) distributes a significant amount of background in the whole region of reconstruction. However, given *a priori* knowledge of the edge of the object, as the object size decreases (e.g., D = 4 cm in Fig. 3), the difference in p(r) between the two systems becomes smaller due to the truncation at smaller radius for p(r). Hence the distribution of noise is dependent on the size of the reconstruction region, and increases for larger objects.

The modulation transfer function (MTF) or frequency content P(ω) of the unfiltered BPSF is given by the two-dimensional Fourier transform (2D-FT) of p. For a rotationally symmetric function such as p, the 2D-FT is given by the Hankel transform:

$$P(\omega) = {}^2\mathcal{F}(p)$$

$$= A\int_0^{D/2} e^{-sr^2} I_0(qr^2) J_0(2\pi r\omega)\, r\,dr \quad (5)$$

where J_0 is the zeroth-order Bessel function of the first kind, ${}^2\mathcal{F}$ is the two-dimensional Fourier transform operator, and A is the renormalizing constant to keep all P(0) = 1.0. Since P(0) represents the integral counts under the point spread function p, all P(ω = 0) should be constant (set to 1.0) to represent identical statistics for systems having different point spread functions. P(ω) can be evaluated numerically, and as an example, the P(ω) for the point spread functions p(r) in Fig. 3 with D equal to 50 cm is shown in Fig. 4.

There are several techniques available for reconstructing an image from its projections. For mathematical simplicity in this study, we have used the prefiltered TOF back-projection image followed by a two-dimensional filtering technique (*5*). The desired reconstruction resolution σ_R(FWHM = Δ_R) is obtained with the appropriate choice of the two-dimensional filter. In the frequency space, the two-dimensional filter F(ω) required to recover a resolution σ_R from the back-projected point spread function p(r) is given by:

$$F(\omega) = P_R(\omega,\sigma_R)/P(\omega,\sigma_{ci},\sigma_{ct},D), \quad (6)$$

where $P_R(\omega,\sigma_R)$ is the two-dimensional Fourier transform of the point spread function $p_R(r,\sigma_R)$ for the desired reconstruction resolution. This point spread function is assumed to be a two-dimensional Gaussian with standard deviation σ_R:

$$p_R(r,\theta_R) = e^{-r^2/2\sigma_R^2};$$

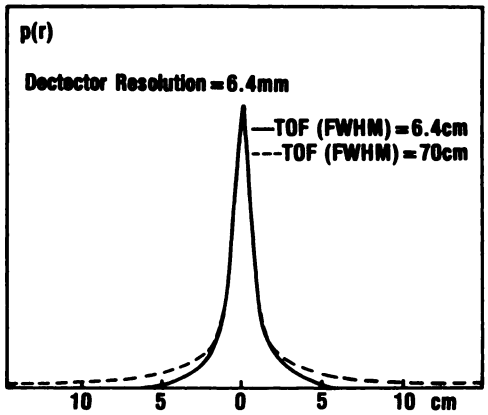

FIG. 3. Point spread functions with TOF FWHM = 6.4 cm and 70 cm, with an intrinsic detector resolution of 6.4 mm.

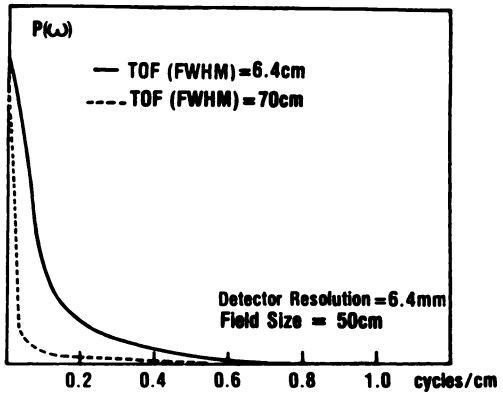

FIG. 4. Two-dimensional fast Fourier Transformation of point spread functions shown in Fig. 3, with field size D = 50 cm.

therefore

$$P_R(\omega,\sigma_R) = e^{-2\pi^2\sigma_R^2\omega^2}. \quad (7)$$

$P_R(\omega,\sigma_R)$ is also renormalized to 1.0 at $\omega = 0$ for the same reason as the P in Eq. 5.

This filtering process to obtain the desired reconstruction resolution modifies the image noise from that of the prefiltered image. If good reconstruction resolution is to be obtained, high-frequency noise in the prefiltered image will be amplified. If low reconstruction resolution is tolerable, the high-frequency noise in the prefiltered image will be suppressed, resulting in an image with lower resolution and less noise.

The total noise variance at the center of a large circular uniform activity distribution after filtering is then calculated as follows. The noise variance partially follows the development of Ref. *3*, extended to include the detector's intrinsic resolution. For a measured event at the center of the object (0,0) as detected by a pair of detectors along the x direction (Fig. 2) with confidence weighting, an intensity distribution of

$$p_0 = e^{-x^2/2\sigma_t^2 - y^2/2\sigma_i^2} \quad (8)$$

is projected. For a detection line along another angle θ, one can find p_θ by rotating p_0 by θ

$$p_\theta = p_0(x\cos\theta + y\sin\theta, -x\sin\theta + y\cos\theta) \quad (9)$$

Therefore the measured activity at the origin by the detector pair at angle θ contributes an image intensity $p(x,y,\theta)$ at (x,y):

$$p(x,y,\theta) = ap_0(x\cos\theta + y\sin\theta, -x\sin\theta + y\cos\theta)**f(r), \quad (10)$$

where f(r) is the desired filter and "a" is the measured number of counts at the center

$$p(x,y,\theta) = a\int_{-\infty}^{\infty}\int_{-\infty}^{\infty} \times p_0\{(x-x')\cos\theta + (y-y')\sin\theta - (x-x')\sin\theta + (y-y')\cos\theta\} \times f(\sqrt{(x'^2+y'^2)})\,dx'dy'$$

Let $s = x'\cos\theta + y'\sin\theta$, and $t = -x'\sin\theta + y'\cos\theta$,

$$p(x,y,\theta) = a\int_{-\infty}^{\infty}\int_{-\infty}^{\infty} \times p_0(x\cos\theta + y\sin\theta - s, -x\sin\theta + y\cos\theta - t)\cdot f(\sqrt{(s^2+t^2)})\,dsdt$$

$$p(x,0,\theta) = a\int_{-\infty}^{\infty}\int_{-\infty}^{\infty} p_0(x\cos\theta - s, -x\sin\theta - t)f(\sqrt{(s^2+t^2)})\,dsdt = a\{p_0**f\}(x\cos\theta, -x\sin\theta) \quad (11)$$

Hence, the variance at $(x,0,\theta)$:

$$V(x,0,\theta) = \overline{\{\Delta p(x,0,\theta)\}^2} = \overline{\{\Delta(a(p_0**f)(x\cos\theta, -x\sin\theta))\}^2} = \{(p_0**f)^2(x\cos, -x\sin\theta)\}\cdot\overline{(\Delta a)^2}.$$

Since a, the measured counts at (0,0) by the detector pair at angle θ, follows Poisson statistics,

$$V(x,0,\theta) = a(p_0**f)^2(x\cos\theta, -x\sin\theta). \quad (12)$$

The variance contribution at (x,0) from all the detection angles is then:

$$V(x,0) = \int_0^\pi V(x,0,\theta)\,d\theta = \bar{a}\int_0^\pi (p_0**f)^2(x\cos\theta, -x\sin\theta)\,d\theta \quad (13)$$

Since the equation is nothing but the 2-D back-projection of $(p_0**f)^2$, and the results have only r-dependence,

$$V(r) = \bar{a}R\{(p_0**f)^2\}(r). \quad (14)$$

For a large uniform object, the contribution of the noise variance to r from the measured counts at the origin is equivalent to the contribution of the measured activity at r to the origin. Hence, the total noise contribution at the origin from the surrounding activity is

$$V(0) = \bar{a}\int_0^\infty\int_0^\pi R\{(p_0**f)^2\}(r)\,rdrd\theta.$$

Applying Parseval's theorem (*3*):

$$V(0) = \pi\bar{a}\int_0^\infty R\{(P_0F)^2\}(\omega)\,\omega d\omega,$$

where P_0 and F are the two-dimensional Fourier transforms of the weighting function p_0 and the filter function f.

Since F from Eq. 6 has rotational symmetry,

$$V(0) = \pi\bar{a}\int_0^\infty F^2R\{P_0^2\}(\omega)\,\omega d\omega. \quad (15)$$

This is the noise variance for an infinite or large uniform activity distribution. It can be used, however, to approximate that of a finite uniform distribution, since with the currently available TOF detector timing, the contribution of noise at (0,0) from events near or outside the practical range of object perimeter is negligble. This approximation will not hold, however, for small object size D relative to the TOF resolution. Hence, all calculations presented in the following restrict the TOF resolution FWHM $\Delta_t < D/3$: for a D = 20 cm, $\Delta_t(\max)$ = 0.5 nsec; for D = 30, $\Delta_t(\max)$ = 0.7 nsec and for D = 40 cm, $\Delta_t(\max)$ = 1 nsec. Equation 15 has a simple physical interpretation. Since every count collected is weighted by the weighting function p_0, it is equivalent to convolving the data by p_0. The convolution changes the noise

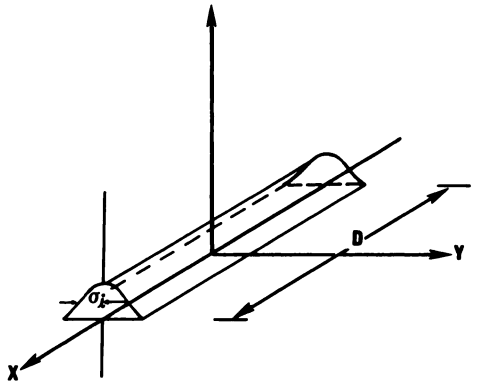

FIG. 5. Weighting function with infinite time-of-flight, finite detector size (s.d. = σ_i), and known activity diameter D.

spectrum from that of the sampling pixel's size to that of the detection-uncertainty size. In other words, the noise band-pass is restricted and equal to P_0, the 2D-FT of p_0. Moreover, if F is equal to unity (i.e., if no filtering takes place):

$$V(0) = \pi\bar{a} \int_0^\infty R\{P_0^2\}(\omega)\, \omega d\omega.$$

Hence, $R\{P_0^2\}$ and F^2 can be interpreted as the noise power spectrum defined by the detector uncertainty before filtering and the noise amplification of the filter respectively. Hence, the variance V(0) is given by the integration of [noise spectrum] × [noise amplification] over the entire frequency space.

To compare the S/N between TOF and the conventional PET systems, Eq. 15 is also used to calculate the noise variance of the conventional systems.

In the conventional system, the prefiltered noise spectrum $R(P_0^2)$ in Eq. 15 can be found analytically as follows. The weighting function is as shown in Fig. 5.

$$p_0 = \begin{cases} e^{-y^2/2\sigma_i^2} & |x| \le D/2 \\ 0 & |x| > D/2 \end{cases}$$

$$P_0 = \int_{-\infty}^{\infty}\int_{-\infty}^{\infty} p_0 \; e^{-2\pi i(ux+vy)}\, dxdy \qquad (16)$$

$$= \int_{-D/2}^{D/2} e^{-2\pi iux} \; e^{-2\pi^2\sigma_i^2 v^2}\, dx$$

$$= e^{-2\pi^2\sigma_i^2 v^2} \; \frac{\sin(\pi Du)}{\pi u}$$

$$R\{P_0^2\} = \frac{2}{\pi}\int_0^{\pi/2} \times e^{-4\pi^2\sigma_i^2\omega^2\sin^2\theta\{\sin^2(\pi D\omega\cos\theta)/\pi^2\omega^2\cos^2\theta\}}\, d\theta$$

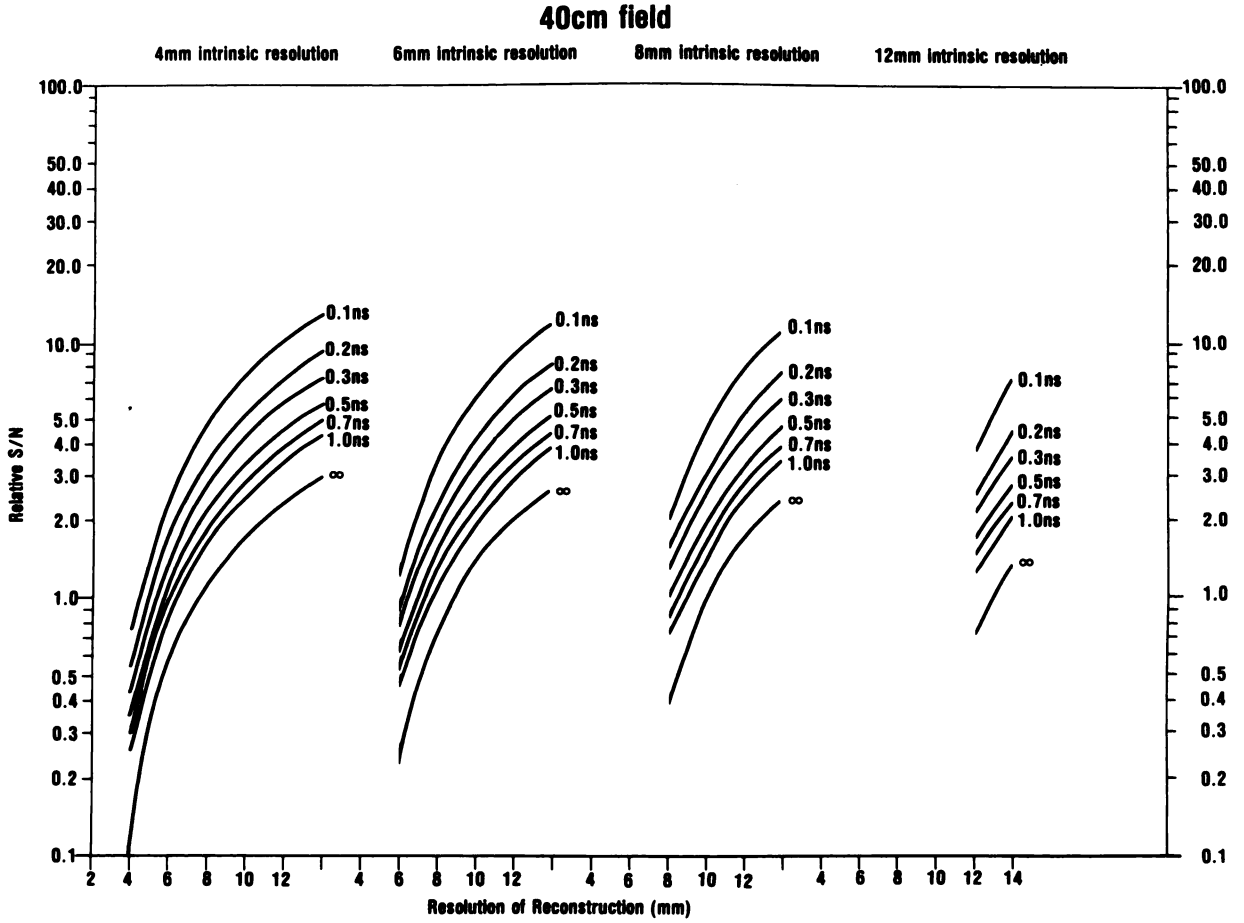

FIG. 6. Relative signal-to-noise ratios for uniform source 40 cm in diameter, as functions of detector's intrinsic resolution, TOF resolution, and reconstructed resolution.

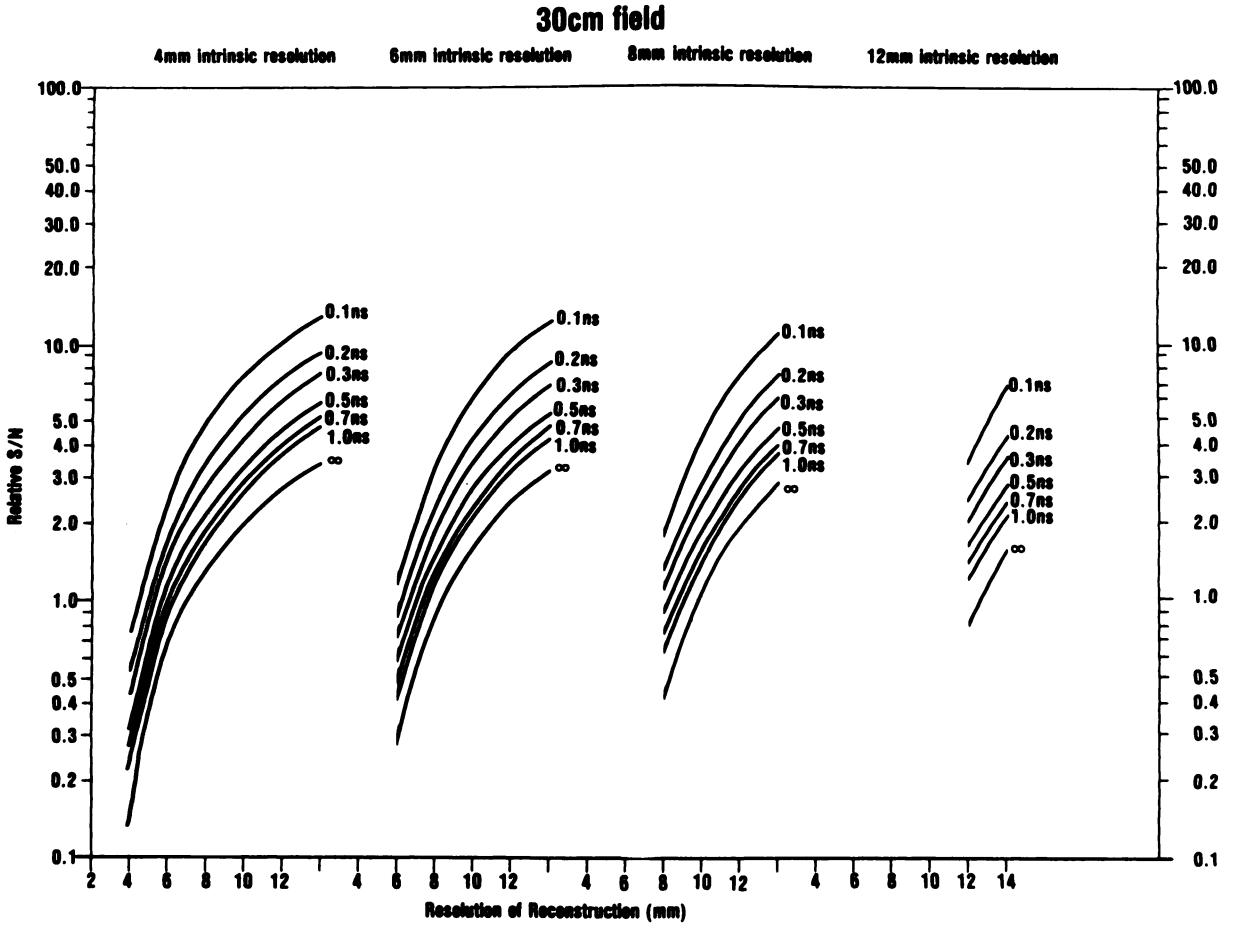

FIG. 7. Relative signal-to-noise ratios for uniform source 30 cm in diameter, as functions of detector's intrinsic resolution, TOF resolution, and reconstructed resolution.

Using the above Eqs. 15, 16, 6, and 5, the relative noise variance or relative signal to noise ratio, S/N, is calculated as a function of σ_t, σ_i, σ_r, D. Relative S/N is defined as: $S/N = 1/\sqrt{V(0)}$.

RESULTS

Using the above equations we have calculated numerically the relative S/N as a function of σ_c, σ_I, σ_R, D. The calculations are carried out for three different activity sizes: D = 20 cm, 30 cm, and 40 cm. For each activity size D, four values of detector intrinsic resolutions with FWHM (Δ_i) equal to 4, 6, 8, and 12 mm were used, and for each D and Δ_i, the TOF resolution FWHM, Δ_t, was varied from 0.1 nsec to the Δ_t (max) as discussed earlier, together with the non-TOF conventional limit. A relative S/N was then calculated for each D, Δ_i, and Δ_t, for a range of recovered reconstructed resolution from 4 to 14 mm (FWHM). As an example, Fig. 6 shows the relative S/N for a 40-cm uniform activity source, plotted as a function of the recovered resolution for different intrinsic detector resolutions and several TOF values. Figures 7 and 8 show similar calculations for object sizes of 30 and 20 cm. To simplify the results we have assumed constant slice thickness and detection efficiency for each size of detector. For instances in which slice thickness or detection efficiency change, the relative S/N can be estimated to be higher or lower with a multiplicative factor derived from the detection efficiency of a particular detector and scanner geometry.

The S/N curves for TOF Δ_t = 0.1–0.5 nsec for all three object sizes are almost identical, since $\sigma_t \ll D$ and the effect of the object-edge truncation for the point spread function is negligible. Most of the variation in S/N curves between the different object sizes comes from the conventional-system calculations for various intrinsic detector resolutions. Since the large object sizes of 30 and 40 cm allow the noise variance (Eq. 15) to approximate that of a finite object even for worse TOF resolution, TOF σ_t = 0.7 nsec was added for the 30-cm object and σ_t = 0.7, 1.0 nsec was added for the 40-cm object. These calculations have been verified for the relative S/N with Ref. *4*, which exactly calculates the finite-object noise variance for the case of a 30-cm object. The calculation for σ_i = 8 mm is presented in the comparison. For all the cases studied here it is interesting to observe that in the conventional system, the S/N decreases asymptoticaly much faster than that of the TOF

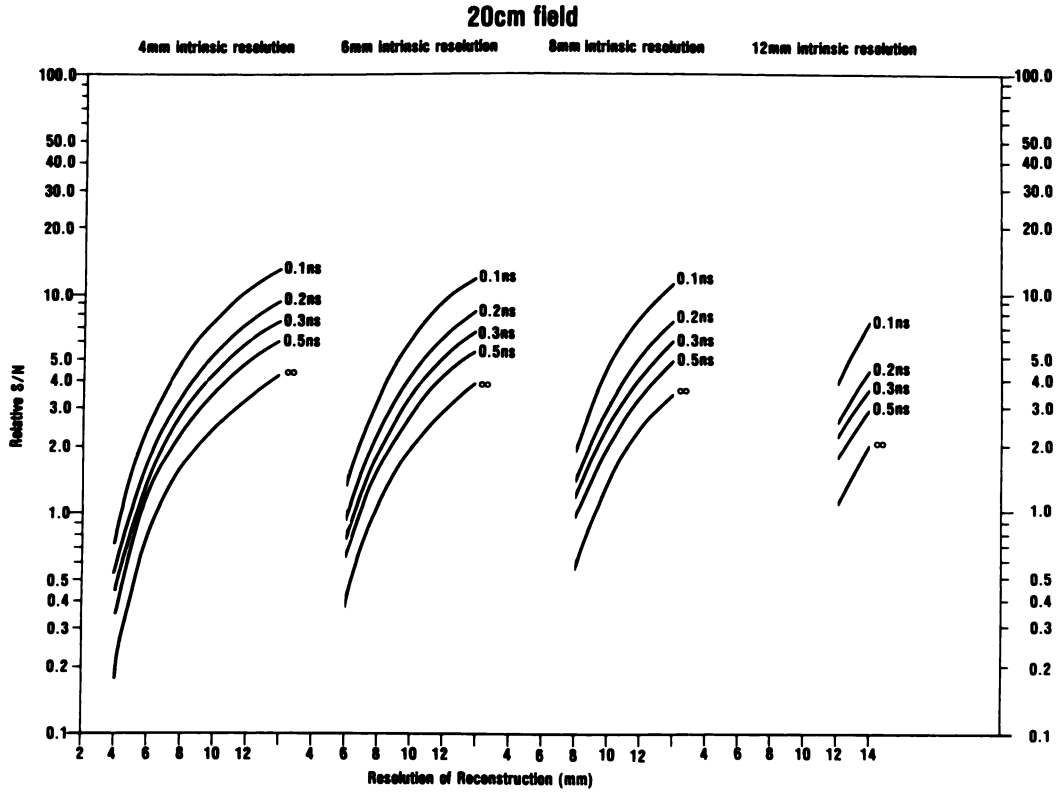

FIG. 8. Relative signal-to-noise ratios for uniform source 20 cm in diameter, as functions of detector's intrinsic resolution, TOF resolution, and reconstructed resolution.

system as one tries to reconstruct to resolutions smaller than 1.2 times the IR. Hence, it indicates that the TOF system that may be reconstruct to slightly higher resolution than that of a similar conventional systems. These calculations also show that a gain in relative S/N can be achieved by using detectors smaller than the desired reconstruction resolution as in Refs. *6* and *7*. This is easily understandable, since from Eqs. 6 and 15:

$$V(0) = \pi\bar{a} \int_0^\infty \frac{P_R^2(\omega,\sigma_R)}{P^2(\omega)} R\{P_0^2\}(\omega)\, \omega d\omega,$$

and

$$\begin{aligned} P^2 &= (^2f\{p\})^2 \\ &= \{^2f R(p_0 ** p_0)\}^2 \\ &= \{R(P_0^2)\}^2. \end{aligned}$$

Hence,

$$V(0) = \pi\bar{a} \int_0^\infty \frac{P_R^2(\omega,\sigma_R)}{R(P_0^2)} \omega d\omega,$$

and for any reconstruction resolution σ_R, the noise variance V(0) will be lower if $R(P_0^2)$ is larger at all values of ω. This in turn implies smaller detector intrinsic size and/or TOF variance in the spatial domain.

DISCUSSION

These results can be used to evaluate the relative importance of the detector's intrinsic resolution and TOF resolution for a given size of activity distribution, so that a better optimization between these two important parameters can be obtained in regard to the available detector competence. For example, some of the results shown in Figs. 6, 7, and 8 are extrapolated and replotted in Figs. 10, 11, and 12 respectively for discussion.

For the 40-cm field size, as shown in Fig. 10, useful TOF S/N gain can be obtained with a TOF resolution of 500–600 psec. If one is to decide between a 4-mm-IR non-TOF system and a 8-mm-IR 550-psec TOF system with identical detection efficiency, the former will be a

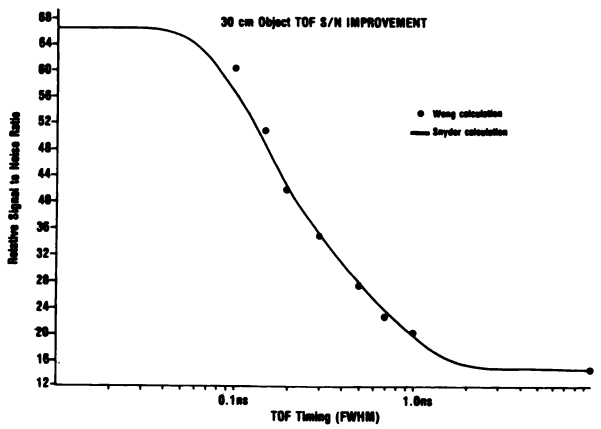

FIG. 9. Comparison of present calculation with that of Ref. 4 for special case of a 30-cm object.

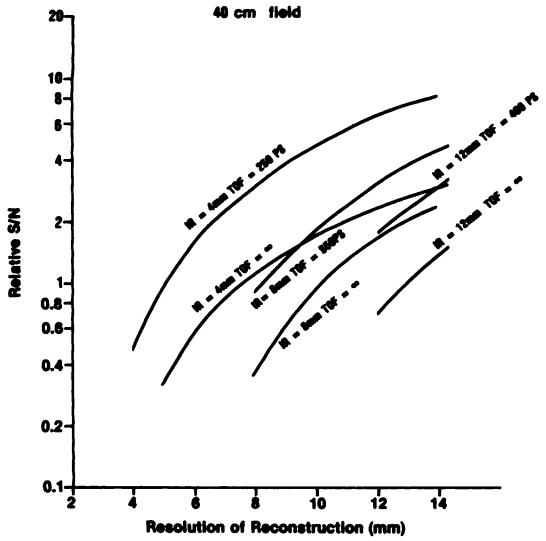

FIG. 10. Forty-cm object; relative S/N comparison among six chosen systems: 4-mm-IR, 6-mm-IR conventional, 8-mm-IR TOF, 12-mm-IR TOF, and a standard 12-mm-IR conventional system.

better choice provided that good reconstruction resolution (<8 mm) is needed and the low S/N or sensitivity associated with such small reconstruction resolution is tolerable. This is often the case in a research environment. On the other hand if one needs high S/N or sensitivity and 8–11 mm image resolution is sufficient, the 8-mm-IR 550-psec TOF system is also a viable choice. It can also be observed in Fig. 10 that the 8-mm 550-psec TOF system has a higher S/N than the 12-mm 450-psec TOF system. Hence, in this case, the gain in S/N with the use of smaller detectors more than offsets the loss

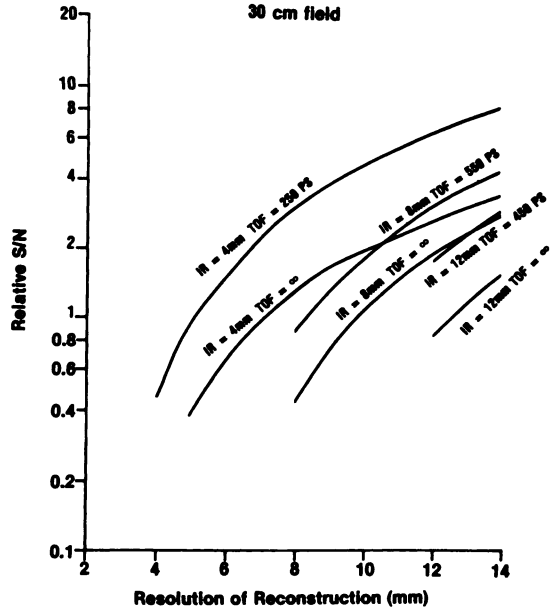

FIG. 11. Thirty-cm object; relative S/N comparison among six chosen systems: 4-mm-IR, 6-mm-IR conventional, 8-mm-IR TOF, 12-mm-IR TOF, and a standard of 12-mm-IR conventional system.

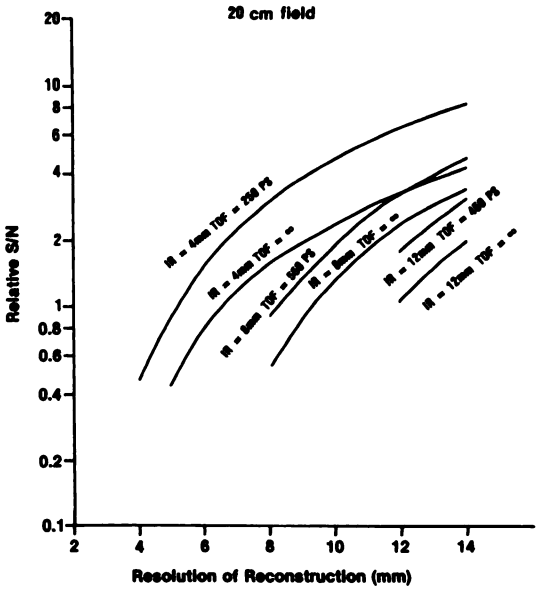

FIG. 12. Twenty-cm object; relative S/N comparison among six chosen systems: 4-mm-IR, 6-mm-IR conventional, 8-mm-IR TOF, 12-mm-IR TOF, and a standard 12-mm-IR conventional system.

resulting from the worse TOF resolution. The futuristic 4-mm-IR 250-psec TOF system illustrated in Fig. 10 shows that it can reconstruct to 5-mm resolution with the same S/N or sensitivity as that of the 4-mm-IR non-TOF system reconstructing to 7.6 mm.

As the field size decreases to 20 cm, as shown in Fig. 12, the TOF S/N gain is less than that of the 40-cm field size, and the relative merit of using smaller detectors increases. For example, the 4-mm-IR non-TOF system for this small field size has higher S/N throughout the useful region of reconstruction resolution than the 8-mm 550-psec TOF system. However, even at this unfavorable object size for the TOF systems, a TOF resolution of 250 psec can still provide a twofold increase in S/N, or a fourfold increase in sensitivity, over the non-TOF systems, as illustrated by the 4-mm-IR calculations.

Again, one should be cautioned that for more realistic comparisons, one should apply a mutiplicative factor to the present S/N results in order to take into account the actual system differences in detector efficiency, packing fraction, detector ring diameter, slice thickness, and the utilization of all the cross-slice coincidences (*8*). The highly individual system-related factors such as scattered and random coincidence should also be considered when evaluating a particular PET system.

ACKNOWLEDGMENT

This work has been carried out as a joint collaborative research project with the Clayton Research Foundation, Houston, Texas.

APPENDIX 1

The following proof follows that of the 1-D confidence weighting of Ref. *3* but extended for 2-D confidence weighting. The weighted

point spread function p(r) in Eqs. 3 and 4 for any arbitrary 2-D weighting function $w_0(x,y)$ is given by:

$$p(r) = R(p_0(\sigma_i,\sigma_t,D)^{**}W_0)$$

where R is the 2-D back-projection operator

$$\begin{aligned} P(\omega) &= {}^2\mathcal{F}\{p(r)\} = {}^2\mathcal{F}R(p_0{}^{**}W_0) \\ &= R^2\mathcal{F}(p_0{}^{**}w_0) \\ &= R\{P_0 \cdot W_0\} \end{aligned}$$

The filter function F in Eq. 6:

$$F(\omega) = \frac{P_R(\omega,\sigma_R)}{R\{P_0W_0\}}$$

Where P_R is the 2-D-FT of the desired reconstruction resolution point spread function. The variance at the center of the object is given by Eq. 15.

$$\begin{aligned} V(0) &= \int_0^\infty F^2R\{W_0{}^2\}(\omega)\,\omega d\omega \\ &= \int_0^\infty \frac{P_R{}^2(w,\sigma_R)}{\{R(P_0 \cdot W_0)\}^2} R\{W_0{}^2\}(\omega)\,\omega d\omega. \end{aligned}$$

By Schwartz's inequality

$$\begin{aligned} &\{R(P_0W_0)\}^2 \\ &= \left\{\int_0^\pi P_0(\omega\cos\theta,\omega\sin\theta)W_0(\omega\cos\theta,\omega\sin\theta)d\theta\right\}^2 \\ &\qquad \le \{R(P_0{}^2\} \cdot \{R(W_0{}^2)\} \end{aligned}$$

$$V(0) \le \int_0^\pi \frac{P_R{}^2(w,\sigma_R)R(W_0{}^2)}{R(P_0{}^2)R(W_0{}^2)}\,\omega d\omega, \qquad \text{(A1)}$$

the equality holds if $P_0 = W_0$. Therefore, V_{min} occurs when the 2-D weighting function is equal to the 2-D detector's uncertainty function, which is equal to a 2-D Gaussian with the x-y standard deviations equal to the detector's intrinsic resolution σ_i and the time-of-flight resolution σ_t.

APPENDIX 2

For a very large object, a point source at the center of the field is given by:

$$p = \frac{1}{\pi}\int_0^\pi e^{-r^2\cos^2\beta(2\sigma_{ct}{}^2)}\, e^{-r^2\sin^2\beta/(2\sigma_{ci}{}^2)}\, d\beta$$

$$= \frac{2}{\pi} e^{-r^2/(2\sigma_{ci}{}^2)} \int_0^{\pi/2} e^{-r^2(\cos^2\beta)(1/\sigma_{ct}{}^2 - 1/\sigma_{ci}{}^2)/2}\, d\beta.$$

Let $a = r^2(1/\sigma_{ci}{}^2 - 1/\sigma_{ct}{}^2)/2$:

$$p = \frac{2}{\pi} e^{-r^2/(2\sigma_{ci}{}^2)} \int_0^{\pi/2} e^{a\cos^2\beta}\, d\beta.$$

Let $\theta = 2\beta$:

$$\begin{aligned} p &= e^{-r^2/(2\sigma_{ci}{}^2)}\, e^{a/2} \int_0^\pi e^{(a\cos\theta)/2}\, d\theta \\ &= e^{-r^2/(2\sigma_{ci}{}^2)}\, e^{a/2}\, I_0\{a/2\}, \end{aligned}$$

where I_0 is the zeroth-order modified Bessel function of the first kind.

$$p = e^{-r^2(1/\sigma_{ci}{}^2 + 1/\sigma_{ct}{}^2)/4}\, I_0\{r^2(1/\sigma_{ci}{}^2 - 1/\sigma_{ct}{}^2)/4\}$$

REFERENCES

1. ALLEMAND R, GRESSET C, VACHER J: Potential advantages of a cesium fluoride scintillator for a time-of-flight positron camera. *J Nucl Med* 21:153–155, 1980
2. MULLANI N, MARKHAM J, TER-POGOSSIAN MM: Feasibility of time-of-flight reconstruction in positron emission tomography. *J Nucl Med* 21:1095–1097, 1980
3. TOMITANI T: Image reconstruction and noise evaluation in photon time-of-flight assisted positron emission tomography. *IEEE Trans Nucl Sci* NS-28 4582–4589, 1981
4. SNYDER DL, THOMAS LJ, TER-POGOSSIAN MM: A mathematical model for positron-emission tomography for time-of-flight measurements. *IEEE Trans Nucl Sci* 1029–1033, 1982
5. PHILIPPE EA, MULLANI N, HARTZ R, et al: Real-time image reconstruction for time-of-flight positron emission tomography (TOFPET). *IEEE Trans Nuc Sci* NS-29, 524–528, 1982
6. CHESLER DA, RIEDERER SJ, PELC NJ: Noise due to photon counting statistics in computed x-ray tomography. *J Comput Assist Tomogr* 1:64–74, 1977
7. PHELPS ME, HUANG SC, HOFFMAN EJ, PLUMMER D, CARSON R: The signal amplification technique (SAT): An approach for improving resolution and reducing image noise in computed tomography. *J Comput Assist Tomogr* 6:551–555, 1982
8. MILANI N, WONG WH, HARTZ R, et al: Sensitivity improvement of TOFPET by the utilization of the inter-slice coincidences. *IEEE Nucl Sci Symp* NS-29, 479–483, 1982